Monitoring orbital precession of EO-1 Hyperion with three atmospheric correction models in the Libya-4 PICS

Christopher Neigh[1*], Joel McCorkel[1], Petya Campbell[1,2], Laurence Ong[1,3], Vuong Ly[4], David Landis[1,5], Stuart Fry[1,6], and Elizabeth Middleton[1]

[1] NASA GSFC Biospheric Sciences Laboratory Code 618, Greenbelt, MD 20771 USA
[2] University of Maryland, Baltimore County, Baltimore, MD 21250 USA
[3] Science Systems Applications Inc., Lanham, MD 20706 USA
[4] NASA GSFC Ground Software Systems Branch Code 583 Greenbelt, MD 20771 USA
[5] Sigma Space Corporation, Lanham, MD 20706 USA
[6] Stinger Ghaffarian Technologies, Greenbelt, MD 20770
* Corresponding author

***Abstract*— Spaceborne spectrometers require spectral-temporal stability characterization to aid validation of derived data products. EO-1 began orbital precession in 2011 after exhausting onboard fuel resources. In the Libya-4 Pseudo Invariant Calibration Site (PICS) this resulted in a progressive shift from a mean local equatorial crossing time of ~10:00 AM in 2011 to ~8:30 AM in late 2015. Here, we studied precession impacts to Hyperion surface reflectance products using three atmospheric correction approaches from 2004 to 2015. Combined difference estimates of surface reflectance were < 5% in the visible near infrared (VNIR) and < 10% for most of the shortwave infrared (SWIR). Combined coefficient of variation (CV) estimates in the VNIR ranged from 0.025 – 0.095, and in the SWIR ranged from 0.025 – 0.06, excluding bands near atmospheric absorption features. Reflectances produced with different atmospheric models were correlated (R^2) in VNIR from 0.25 – 0.94 and SWIR from 0.12 – 0.88 ($p < 0.01$). The uncertainties in all models increased with terrain slope up to 15° and selecting dune flats could reduce errors. We conclude that these data remain a useful resource over this period.**

Index Terms—pseudo-invariant calibration site (PICS), land surface imaging (LSI), EO-1 Hyperion, surface reflectance, Libya-4, time-series analysis, ATREM, ACORN, FLAASH, orbital precession

I. INTRODUCTION

Analysis of EO-1 Hyperion high spectral resolution imagery (0.4 – 2.5 μm) is needed to link data products for cross-calibration [1]. These data could be used for multi-spectral data replication, or for on orbit cross-calibration among satellite instruments [1-4] to create a land surface imaging (LSI) virtual constellation approach of merging similar but disparate satellite records. Estimating trends in Hyperion products due to precision could support future LSI studies, as the LSI virtual constellation concept is only viable if the stability of constituents is known with uncertainties.

EO-1 Hyperion currently has the longest spaceborne spectrometer record extending more than 15 years. Launched in 2000, EO-1 was a one-year technology demonstration mission, but it was extended multiple times [5]. It has been useful for testing new technologies implemented in current missions (e.g., Landsat-8) and future missions including the Hyperspectral Infrared Imager (HyspIRI) and the German satellite EnMAP [5]. End of mission is projected for late 2016 due to a local equatorial overpass time earlier than 8 AM.

Hyperion has been used widely for a number of different studies [5] with recent examples including the mapping of land-cover land-use change [6-8] and disturbances [9]; volcanoes and geology [10, 11]; water resources [12]; evaluating seasonal dynamics at pseudo invariant calibration sites (PICS) and vegetated eddy covariance sites [13]; as well as algorithm evaluations [14-17] with many more uses not mentioned here. The utility of Hyperion for cross-calibration has gained interest in recent mission years [18, 19] and archived data could be useful

for many years to come. For this reason among others, a need exists to characterize orbital precession impacts to products in the latter EO-1 operational years (2011-2016).

A number of recent studies have used Hyperion for cross-calibration. For example: Angal *et al.* [20] used Hyperion images to cross calibrate Landsat 7 with the Terra satellite's Moderate Resolution Imaging Spectroradiometer (MODIS) data using the Committee on Earth Observing Satellites' (CEOS) Libya-4 PICS, finding that surface spectral reflectances were consistently within 7% after band adjustments were made. Angal *et al*. [19] also used Hyperion images to cross-calibrate Landsat 5, Landsat 8, and Aqua MODIS reflectance to within 4%. Mishra *et al*. [18] used Hyperion data to extend a cross-calibration model through visible and near-infrared (VNIR) wavelengths for the Landsat 7 Enhanced Thematic Mapper + found accuracies of 3% with an uncertainty of ~2%. As noted in our prior study, Neigh *et al.* [21] found that dune peaks have higher surface reflectance originating from sand properties related to grain size, shape and composition [22, 23], whereas dune ridges have more variability in BRDF due to shadowing [24]. These studies incorporated Hyperion's narrow band VNIR and shortwave infrared (SWIR) spectrum to improve cross calibration estimates among other satellite sensors. Estimating the effects of EO-1 precession on Hyperion's reflectance at Libya-4 will be useful to other Earth observing AM-train missions that are reaching end of life, because their orbits and data products may degrade in a similar manner.

Libya-4 is part of the Sahara desert, commonly referred to as the "seas of sand" (see Fig. 1 from Neigh *et al.* [21]), and has a mean terrain height of 113 m above sea level. Typically, atmospheric aerosols and cloud cover are low, making it an ideal location for cross comparing Earth-observing sensors. Many large irregular North to South dunes transect the region, with some ridges > 70 m in height (Fig 1). In 2015, Govaerts [24] used the Advanced Spaceborne Thermal Emission and Reflection Radiometer (ASTER) Global Digital Elevation Model (GDEM) in Raytran (three-dimensional radiative transfer model) simulations and concluded that dune size and orientation can produce BRDF effects from seasonal solar zenith angle and azimuth angles changes. Even with these large dunes, Helder *et al.* [25] found Libya-4 to be one of the best cross calibration sites due to high reflectance throughout the visible and shortwave infrared (VSWIR) spectrum, with temporal variability of < 2.3% from 48 multi-spectral radiometricly corrected (Level 1R) Landsat 5 images. Bhatt *et al.* 2014 [26] found Libya-4 to be temporally stable within 1% and to exhibit homogeneity (SD, 1.4%) over a decade, as viewed with Aqua MODIS top of atmosphere (TOA) band-1 reflectance (band center 0.65 μm, 250 m resolution). These results suggest Libya-4 is an ideal location to monitor the impacts of orbital precession on Hyperion data products. Other studies have examined the Hyperion TOA VSWIR temporal trend in the Libya-4 PICS and found it to be stable within 2.5 – 5 % in most spectral bands [27]. However, this is the first study, to our knowledge, to examine Hyperion's surface reflectance trends associated with EO-1's rapid orbit degradation years (2014+).

We examined the impacts of orbital precession on the quality of Hyperion VSWIR spectra at the Libya-4 calibration site, for which we had three primary questions:

1) What is the impact of orbital precession estimated with three atmospheric correction models; and are the results similar?
2) How spatially variable are estimates associated with large sand dunes, and how do they impact temporal trends?
3) Can Hyperion imagery collected through 2015 be used for cross-calibration?

II. METHODS AND DATA PROCESSING

A. Hyperion

We acquired near-nadir (± 10°) Hyperion images to minimize bidirectional distribution function (BRDF) effects from large dunes [21, 24]. Hundreds of overlapping Hyperion images are available for the Libya-4 PICS (path 181 row 40) but we used view zenith angle, solar zenith angle seasonality (May through Sept), and cloud screening to select 35 near-nadir images for analysis (Table 1). Hyperion data were not corrected for stripping [28, 29] (detector gains, biases, spectral response functions, nonlinearities, noise, etc.) or other [29, 30]. We applied atmospheric correction routines using Atmospheric REMoval program (ATREM) [31], Atmospheric CORection Now (ACORN) [32] and Fast Line-of-sight Atmospheric Analysis of Spectral Hypercubes (FLAASH) [33, 34] using standard parameters for the Libya-4 PICS with no spectral polishing. ATREM uses a radiation transport (RT) model based on 6S, and ACORN and FLAASH are based on more complex RT models that retrieve atmospheric properties from bands near absorption features [35, 36]. Both ACORN and FLAASH, accounted for the cross-track spectral calibration variation (smile and key stone effects) and used ratiative transfer calculations and the measured, calibrated radiance data to achive a subset of the atmospheric effectspresent in hyperspectral data. The derived atmospheric properties are used in conjunction with modeled atmospheric properties to correct data. All three models use one target location within the image, therefore, in a diverse terrain the reflectance estimates are most accurate closer to the specified location. More model information is provided in Kruse [34] and Gao et al. [37]; and parameters were consistently applied through time (Table 1).

Hyperion surface reflectances were co-registered to a Global Land Survey Landsat 8 level 1 terrain corrected image, using Environment for Visualizing Images (ENVI) software. More than 25 tie points were collected per image and the maximum tie-point root mean square error (RMSE) was 0.6 m. We subset the imagery to a consistent area overlapping high spatial resolution WorldView (WV) satellite data, located at the central lower left portion of the Hyperion image strip. We estimated the combined atmospheric model uncertainty using a quadrature (Q) statistic [38], expressed as the square root of the coefficient of variation (CV) of the sum of squares from ATREM (AT), ACORN (AC) and FLAASH (F) described in equation 1:

$$Q = \sqrt{AT_{cv}^2 + AC_{cv}^2 + F_{cv}^2} \quad (1)$$

Surface reflectance coefficient of determinations (R^2, $p < 0.01$) *w*ere also *calculated as pair-wise combinations between models.*

B. Terrain geometry from WorldView-1 and WorldView-2

WorldView (WV) data were obtained through a license agreement that the National Geospatial Intelligence Agency (NGA) established with DigitalGlobe [39]. The temporal and stereoscopic satellite geometry match of August 11th 2012 for WV-1 and WV-2 provided the opportunity to produce a digital terrain model (DTM) from the 0.5-m resolution panchromatic bands allowing estimation of the impact of terrain height and slope. More details about how this DTM was processed is available in Neigh *et al.* [21]. This resulted in a sample consisting of 9.7×10^4 pixels for analysis through 35 time-steps.

III. RESULTS AND DISCUSSION

A. Hyperion Trend Analysis

Our results appear consistent with other studies that found Hyperion TOA radiances to be spectrally stable within 5% in the VNIR and 10% in the SWIR [27]. Figure 2 displays trends,

CV, and R^2 (p-val < 0.01) for reflectance in 172 calibrated bands retrieved with AT, AC and F models. VNIR reflectance from the AT model showed small (< 2%) reductions and was nearly identical to AC or F models, and showed a slightly larger trend reduction (~10%) at all but a few wavelengths at the edge of atmospheric features, especially for the AC model (Fig. 2A). Trend values in the SWIR region were closer among models, except for the F model at wavelengths < 2050 nm. This difference in reflectance retrievals among models produced variable Q uncertainties across the spectrum. Based on the AT model alone, a smaller uncertainty would be computed for this desert site. The CVs for reflectance computed from all three models were similarly low (< 5%) for most wavelength regions (e.g., 450 – 900 nm; 1500 – 1800 nm; 2050 – 2400 nm) except for wavelengths at the edges of atmospheric features where variable F model values were higher, contributing to higher Q for the CVs at those wavelengths (Fig. 2b). The strongest pair-wise correspondence between models throughout the VSWIR was AC vs. F and AT vs. F models, with some of the strongest correspondence for reflectance retrievals for AT vs. F models in the VIS and SWIR (Fig. 2c).

The trends through time were examined for the mean surface reflectance retrievals for 25 selected wavelengths obtained with the three models (Fig. 3). The temporal anomaly trend was low (< ~5%) for most of these models and bands. We did not find any significant or rapid degradation from 2011 through the summer of 2015 in any product. This is expressed in the flat trends (slope of regression line ≈ 0) through time for all examined wavelengths. Hyperion signal-to-noise ratio (SNR) was originally ~150 in the VIS and < 110 in the SWIR [2, 34]; and is declining with an earlier overpass time. Nevertheless, the earlier overpass time reduced the observed surface reflectance by < 10%, because the models account for overpass time and reduced solar energy from precession.

B. WorldView DTM

To understand impacts of large dunes on surface reflectance trends we used the WV derived DTM to group data by dune slope ranging from 0 to 40°. We found spectrally disparate areas for cross-calibration. Our comparison analysis correlated surface reflectance models on a per-pixel basis in 0.05° slope increments, excluding trends with p-val < 0.01. When Hyperion viewed dune regions associated with different degrees of sloping ($0 – 40^o$), there were noticeable differences among the 3 atmospheric correction models in NIR and SWIR wavelengths, and the most consistent retrievals were made in relatively flat regions (~$0 – 10^o$ slope). At slope angles > 15^o, a peak value in the anomaly trend was observed at many wavelengths. The results for the same 25 selected bands show that the spatial variability of the dune peaks is higher than dune flats (Fig. 4). Trends for these bands progressively increased up to 15° then became highly variable, oscillating 2 – 5% in the VIS and >20% in the SWIR. This is because Hyperion imaged both the illuminated and shaded portions of steep dune ridges through time, for which the illuminated vs. shaded proportions varied depending upon satellite viewing geometry. We found steep ridges illuminated from the West typically had positive trends while steep ridges from the east had negative trends. This could also be due to instrument detector and model product differences.

C. Impacts to LSI cross-calibration techniques

Our study identified spatial, temporal and spectral differences within the Libya-4 PICS. We attempted to minimize other issues that included:

1) Co-registration error between products in the time-series: minimized by identifying identical points in Hyperion data, but selecting identical features distributed throughout

the images was difficult in dunes, which lack small descriptive features. We estimate this error to be minimal;

2) The seasonal BRDF effects between images were reduced but not completely ameliorated due to the differences in image acquisition time and viewing geometry;
3) Hyperion detector degradation affects our study by an unknown amount. Calibration coefficients were provided with "at launch" conditions, and images were not de-stripped;
4) The WV DTM defined our study area that occurred towards the center of the Hyperion swath on the image edge. This position within the swath could limit our assessment of cross-calibration due to detector differences by an unknown amount.

Our results suggest that Hyperion is stable in most bands (< 5% VNIR, and < 10% SWIR) from 2004 through 2015 in the Libya-4 PICS. Our results have implications to cross-calibration modeling approaches that use the Libya-4 PICS at moderate 30 m resolution. These approaches that require a time-series to minimize BRDF error could instead use VSWIR information from Hyperion in dune flats to reduce errors in satellite sensor cross-calibration efforts.

IV. CONCLUSION

When using Hyperion surface reflectance products for cross-sensor calibration, pixels used should be co-registered and sub-sampled to specific flat portions of the site to reduce sand dune BRDF impacts. These results are similar to cross-calibration results from Neigh *et al*. [21], and to modeled results from Govaerts [24], but here are confirmed through a time-series. Using dune flats could greatly improve the possibilities of developing a robust cross-calibration model.

We had three primary questions in this study and provide the following answers:

1) What is the impact of orbital precession with three atmospheric correction models; and are results similar? We found when averaged over our study site and between correction models in *Q*, Hyperion in most bands had < 5% negative trend in the VNIR and < 10% in the SWIR. This change is consistent in performance with other Earth observing satellites that investigated TOA radiances over this period [40].
2) How spatially variable are model estimates from large sand dunes and how do they impact temporal trends? Trend estimates in most bands for each atmospheric correction approach have a CV up to ~5% in the VSWIR and most bands have a CV < 2.5%. The greatest CV is within the tails of the imaged spectra, near absorption features and spatially located on steep eastern dune ridges. CV for each model is greatest near these features and propagate into *Q*.
3) Can Hyperion imagery acquired through 2015 be used for cross-calibration? Even with variability introduced from precession, surface topography, detector stripping, co-registration error, and other factors, Hyperion's spectral coverage and derived surface reflectance products remain a useful tool for land surface characterization and cross-calibration.

We suggest that future studies consider impacts of large dunes in the Libya-4 PICS and quantify surface reflectance estimates with techniques we applied to characterize the orbital precession of EO-1 Hyperion. We also demonstrate that Hyperion data through 2015 remain a useful tool for cross-calibration studies.

ACKNOWLEDGEMENTS

We would like to thank the EO-1 science team for comments that improved the quality of the manuscript. Use of trade names is intended for clarity only and does not constitute an endorsement of any product or company by the federal government.

REFERENCES

[1] M. A. Folkman, J. S. Pearlman, L. B. Liao, and P. Jarecke, "EO-1/Hyperion hyperscpectral imager design, development, charcterization, and calibration," in *Hyperspectral Remote Sensing of the Land and Atmosphere*, Sendai, Japan, 2001.

[2] R. O. Green, B. E. Pavri, and T. G. Chrien, "On-orbit radiometric and spectral calibration characteristics of EO-1 Hyperion derived with an underflight of AVIRIS and in situ measurements at Salar de Arizaro, Argentina," *Ieee Transactions on Geoscience and Remote Sensing,* vol. 41, pp. 1194-1203, Jun 2003.

[3] C. S. R. Neigh, J. McCorkel, and E. M. Middleton, "Quantifying Libya-4 Surface Reflectance Heterogeneity With WorldView-1, 2 and EO-1 Hyperion," *Ieee Geoscience and Remote Sensing Letters,* vol. 12, pp. 2277-2281, Nov 2015.

[4] A. Angal, X. X. Xiong, T. Y. Choi, G. Chander, and A. S. Wu, "Using the Sonoran and Libyan Desert test sites to monitor the temporal stability of reflective solar bands for Landsat 7 enhanced thematic mapper plus and Terra moderate resolution imaging spectroradiometer sensors," *Journal of Applied Remote Sensing,* vol. 4, Apr 14 2010.

[5] E. M. Middleton, S. G. Ungar, D. J. Mandl, L. Ong, S. W. Frye, P. E. Campbell*, et al.*, "The Earth Observing One (EO-1) Satellite Mission: Over a Decade in Space," *Ieee Journal of Selected Topics in Applied Earth Observations and Remote Sensing,* vol. 6, pp. 243-256, Apr 2013.

[6] S. Padma and S. Sanjeevi, "Spectral Matching in Hyperion images for improved characterization of Mangrove ecosystems in southern India," *Multispectral, Hyperspectral, and Ultraspectral Remote Sensing Technology, Techniques and Applications V,* vol. 9263, 2014.

[7] R. George, H. Padalia, and S. P. S. Kushwaha, "Forest tree species discrimination in western Himalaya using EO-1 Hyperion," *International Journal of Applied Earth Observation and Geoinformation,* vol. 28, pp. 140-149, May 2014.

[8] A. Bannari, K. Staenz, C. Champagne, and K. S. Khurshid, "Spatial Variability Mapping of Crop Residue Using Hyperion (EO-1) Hyperspectral Data," *Remote Sensing,* vol. 7, pp. 8107-8127, Jun 2015.

[9] G. Mallinis, G. Galidaki, and I. Gitas, "A Comparative Analysis of EO-1 Hyperion, Quickbird and Landsat TM Imagery for Fuel Type Mapping of a Typical Mediterranean Landscape," *Remote Sensing,* vol. 6, pp. 1684-1704, Feb 2014.

[10] A. B. Pour, M. Hashim, and J. van Genderen, "Detection of hydrothermal alteration zones in a tropical region using satellite remote sensing data: Bau goldfield, Sarawak, Malaysia," *Ore Geology Reviews,* vol. 54, pp. 181-196, Oct 2013.

[11] A. G. Davies, S. Chien, J. Doubleday, D. Tran, T. Thordarson, M. T. Gudmundsson*, et al.*, "Observing Iceland's Eyjafjallajokull 2010 eruptions with the autonomous NASA Volcano Sensor Web," *Journal of Geophysical Research-Solid Earth,* vol. 118, pp. 1936-1956, May 2013.

[12] A. Ozdemir and U. M. Leloglu, "Bathymetry and Water Quality Measurement of Shallow Waters using Hyperion: Sercin Lake," *2014 22nd Signal Processing and Communications Applications Conference (Siu),* pp. 2023-2026, 2014.

[13] P. K. E. Campbell, E. M. Middleton, K. J. Thome, R. F. Kokaly, K. F. Huemmrich, D. Lagomasino*, et al.*, "EO-1 Hyperion Reflectance Time Series at Calibration and Validation Sites: Stability and Sensitivity to Seasonal Dynamics," *Ieee Journal of*

Selected Topics in Applied Earth Observations and Remote Sensing, vol. 6, pp. 276-290, Apr 2013.

[14] Y. F. Bao, C. Y. Yue, and H. Y. He, "An Enhanced Moment Matching method to destriping EO-1/Hyperion data," *Selected Papers from Conferences of the Photoelectronic Technology Committee of the Chinese Society of Astronautics 2014, Pt Ii,* vol. 9522, 2015.

[15] D. R. Thompson, B. J. Bornstein, S. A. Chien, S. Schaffer, D. Tran, B. D. Bue*, et al.*, "Autonomous Spectral Discovery and Mapping Onboard the EO-1 Spacecraft," *Ieee Transactions on Geoscience and Remote Sensing,* vol. 51, pp. 3567-3579, Jun 2013.

[16] M. K. Pal and A. Porwal, "A Local Brightness Normalization (LBN) algorithm for destriping Hyperion images," *International Journal of Remote Sensing,* vol. 36, pp. 2674-2696, 2015.

[17] J. C. Thelen, S. Havemann, and G. Wong, "Surface retrievals from Hyperion EO1 using a new, fast, 1D-Var based retrieval code," *Algorithms and Technologies for Multispectral, Hyperspectral, and Ultraspectral Imagery Xxi,* vol. 9472, 2015.

[18] N. Mishra, D. Helder, A. Angal, J. Choi, and X. X. Xiong, "Absolute Calibration of Optical Satellite Sensors Using Libya 4 Pseudo Invariant Calibration Site," *Remote Sensing,* vol. 6, pp. 1327-1346, Feb 2014.

[19] A. Angal, N. Mishra, X. Xiong, and D. Helder, "Cross-calibration of Landsat 5 TM and Landsat 8 OLI with Aqua MODIS using PICS," in *Earth Observing Systems XIX SPIE*, 2014, pp. 1-9.

[20] A. Angal, X. X. Xiong, A. S. Wu, G. Chander, and T. Choi, "Multitemporal Cross-Calibration of the Terra MODIS and Landsat 7 ETM+ Reflective Solar Bands," *Ieee Transactions on Geoscience and Remote Sensing,* vol. 51, pp. 1870-1882, Apr 2013.

[21] C. S. R. Neigh, J. McCorkel, and E. Middleton, "Quantifying Libya-4 Surface Reflectance Heterogeneity With WorlView-1, 2 and EO-1 Hyperion " *IEEE Geoscience and Remote Sensing Letters,* vol. in press, 2015.

[22] G. Baraboski, B. Kimmel, T. Chen, E. Miranda, and D. Yim, "Effects of sand grain shape on the spectral signature of sandy landscapes in the visible domain," in *International Geoscience and Remote Sensing Symposium (IGARSS)*, Melbourne, Australia, 2013, pp. 3060-3063.

[23] H. Besler, *The Great Sand Sea in Egypt: Formation, Dynamics and Environmental Change - A Sediment-Analytical Approach* vol. 59. Amsterdam, Netherlands: Elsevier, 2008.

[24] Y. Govaerts, "Sand Dune Ridge Alignment Effects on Surface BRF over the Libya-4 CEOS Calibration Site," *sensors* vol. 15, pp. 3453-3470, 2015.

[25] D. L. Helder, B. Basnet, and D. L. Morstad, "Optimized identification of worldwide radiometric pseudo-invariant calibration sites," *Canadian Journal of Remote Sensing,* vol. 36, pp. 527-539, Oct 2010.

[26] R. Bhatt, D. R. Doelling, D. Morstad, B. R. Scarino, and A. Gopalan, "Desert-Based Absolute Calibration of Successive Geostationary Visible Sensors Using a Daily Exoatmospheric Radiance Model," *Ieee Transactions on Geoscience and Remote Sensing,* vol. 52, pp. 3670-3682, Jun 2014.

[27] T. J. Choi, X. Xiong, A. Angal, G. Chnader, and J. J. Qu, "Assessment of the spectral stability of Libya 4, Libya 1, and Mauritania 2 sites using Earth Observing One Hyperion," *Journal of Applied Remote Sensing,* vol. 8, p. 14, 2014.

[28] A. Gerace, J. Schott, M. Gartley, and M. Montanaro, "An Analysis of the Side Slither On-Orbit Calibration Technique Using the DIRSIG Model," *Remote Sensing,* vol. 6, pp. 10523-10545, Nov 2014.
[29] L. X. Sun, R. Neville, K. Staenz, and H. P. White, "Automatic destriping of hyperion imagery based on spectral moment matching," *Canadian Journal of Remote Sensing,* vol. 34, pp. S68-S81, 2008.
[30] R. Bindschadler and H. Choi, "Characterizing and correcting Hyperion detectors using ice-sheet images," *Ieee Transactions on Geoscience and Remote Sensing,* vol. 41, pp. 1189-1193, Jun 2003.
[31] B. C. Gao, K. B. Heidebrecht, and A. F. H. Goetz, "Derivation of Scaled Surface Reflectances from Aviris Data," *Remote Sensing of Environment,* vol. 44, pp. 165-178, May-Jun 1993.
[32] AIG, "Title," unpublished|.
[33] G. W. Felde, G. P. Anderson, T. W. Cooley, M. W. Mathew, S. M. adler-Golden, A. Berk*, et al.*, "Analysis of Hyperion data with the FLAASH atmospheric correction algorithm," in *Geoscience and Remote Sensing Symposium. IGARSS '03*, 2003, pp. 90-92.
[34] F. A. Kruse, J. W. Boardman, and J. F. Huntington, "Comparison of airborne hyperspectral data and EO-1 Hyperion for mineral mapping," *Ieee Transactions on Geoscience and Remote Sensing,* vol. 41, pp. 1388-1400, Jun 2003.
[35] F. A. Kruse, "Comparison of ATREM, ACORN, and FLAASH Atmospheric Corrections using Low-Altitude AVIRIS Data of Boulder, Colorado," in *13th JPL Airborne Geoscience Workshop*, Jet Propulsion Laboratory 2004, pp. 1-10.
[36] B. C. Gao and A. F. H. Goetz, "Column atmospheric water vapor and vegetation liquid water retievals from airborne imaging spectrometer data," *Journal of Geophysical Research,* vol. 95, pp. 3549-3564, 1990.
[37] B. C. Gao, M. J. Montes, C. O. Davis, and A. F. H. Goetz, "Atmospheric correction algorithms for hyperspectral remote sensing data of land and ocean," *Remote Sensing of Environment,* vol. 113, pp. S17-S24, Sep 2009.
[38] J. R. Taylor, *An Introduction to Error Analysis The Study of Uncertainties in Physical Measurements*. United States of America: University Science Books, 1939.
[39] C. S. R. Neigh, J. G. Masek, and J. Nickeson, "High-Resolution Satellite Data Open for Government Research," *EOS Transactions,* vol. 94, pp. 121-123, March 26 2013.
[40] G. Chander, X. X. Xiong, T. Y. Choi, and A. Angal, "Monitoring on-orbit calibration stability of the Terra MODIS and Landsat 7 ETM+ sensors using pseudo-invariant test sites," *Remote Sensing of Environment,* vol. 114, pp. 925-939, Apr 15 2010.

Figure 1. Subsets of the study area shown in 3D: (a) WorldView-1 and 2 derived digital terrain model (DTM); (b) WorldView-2 true color red, green and blue image linear stretched and draped on the DTM © 2012 DigitalGlobe NextView License.; (c) Slope estimates from DTM draped on DTM.

Figure 2. Mean surface reflectances for 172 VSWIR calibrated Hyperion bands for imagery of Libya-4 acquired from 2004 through 2015. Trends in mean surface reflectance determined with three atmospheric correction models ATREM, ACORN, and FLAASH were evaluated: (1st row a) temporal trend means across the spectrum, plus the Q uncertainty statistic; (2nd row, b) coefficient of variation (CV) for temporal trend, plus the Q uncertainty statistics; and (3rd row, c) coefficient of determination (R^2), between pair-wise atmospheric correction models $p < 0.01$ in all cases.

Figure 3. Time-series of the VSWIR surface reflectance anomaly trends for the study area mean from 2004 – 2015 for the three atmospheric correction models (AT, AC, F) in 25 selected bands. The temporal trend is flat (slope ≈ 0, $p < 0.01$) in all cases.

Figure 4. The VSWIR surface reflectance anomaly trends by DTM slope (0 – 40°) obtained from three atmospheric correction models (AT, AC, F) in 25 selected bands. The most consistent results were observed for slopes < 10^o.

TABLE 1

Summary of image attributes (a) and atmospheric correction model parameters (b).

a)

Date		Start T.	Look	Sat.	Solar	Solar
MM-DD	Year-DOY	GMT	Ang.°	Incl.°	Azi.°	Zen.°
Sep-04	2004-250	8:44:35	-0.2	98.2	129.4	32.4
Jul-06	2006-185	8:44:13	-1.3	98.1	98.0	24.3
Jul-06	2006-257	8:44:13	-1.3	98.1	98.0	24.3
Sep-06	2007-151	8:41:11	-7.6	98.1	132.6	34.7
May-07	2007-258	8:45:46	4.2	98.1	102.0	22.9
Sep-07	2008-128	8:41:04	-2.8	98.1	132.8	34.8
May-08	2009-231	8:41:09	-2.7	98.1	111.8	25.9
Aug-09	2010-134	8:43:27	1.5	98.1	117.7	29.2
May-10	2010-147	8:42:38	0.0	98.1	109.0	24.7
May-10	2010-227	8:46:27	7.5	98.1	103.9	22.9
Aug-10	2010-232	8:46:19	7.3	98.1	116.3	28.1
Aug-10	2010-258	8:40:12	-4.9	98.1	117.5	30.0
Sep-10	2011-154	8:47:06	8.7	98.1	135.1	34.0
Jun-11	2011-224	8:42:15	0.4	98.1	100.5	23.6
Aug-11	2011-229	8:43:42	4.3	98.1	113.7	28.2
Aug-11	2011-237	8:36:49	-9.1	98.1	114.5	30.2
Aug-11	2011-242	8:45:11	7.5	98.1	121.9	29.9
Aug-11	2011-255	8:38:16	-6.0	98.1	122.7	32.0
Sep-11	2011-268	8:39:40	-3.0	98.1	130.7	34.4
Sep-11	2012-187	8:40:54	-0.2	98.1	138.0	37.4
Jul-12	2012-208	8:35:35	1.1	98.0	97.0	26.3
Jul-12	2012-221	8:37:57	6.9	98.0	103.9	27.5
Aug-12	2012-242	8:34:39	1.1	98.0	109.4	29.6
Aug-12	2012-255	8:36:32	6.1	98.0	122.0	32.3
Sep-12	2013-170	8:32:53	-0.4	98.0	128.4	35.5
Jun-13	2013-199	8:18:16	-6.8	98.0	93.5	29.1
Jul-13	2013-215	8:16:51	-6.8	98.0	96.9	31.3
Aug-13	2013-228	8:22:29	5.9	98.0	104.1	31.6
Aug-13	2014-251	8:14:48	-8.2	98.0	108.8	34.6
Sep-14	2014-275	7:56:13	3.4	97.9	116.7	41.6
Oct-14	2014-291	7:51:50	-1.8	97.9	127.5	47.1
Oct-14	2014-299	7:48:25	-6.2	98.0	133.0	51.4
Jun-15	2015-155	7:28:39	-3.1	97.9	89.1	39.6
Jun-15	2015-166	7:33:53	9.3	97.9	88.1	38.7
Jul-15	2015-182	7:23:38	-8.4	97.9	88.1	38.7

b)

Model Parameters	ATREM	ACORN	FLAASH
Sens Alt km	695	690 – 695	695
Ground Elv m	118	118	86 – 91
Polishing	off	off	off
Version		6.1	
Mode	—	—	—
Model Loc/Seas		Mid Lat Sum.	
Band Est. Water Vap.	—	940, 1140 nm	—
MODTRAN EXE	—	—	Mod90_5.2.0.0
MODTRAN AER	—	1	1
MODTRAN RES	—	15	15
MODTRAN ATM	—	2	2
MODTRAN MSCAT	—	—	1
CO2_MIXING ppm			390
Default Vis km	40	40	37
Use Adjacency	no	no	2
Use Aerosol	—	1	1
Absorp./Scatt. LUT	—	Modtran 4	

Fig. 1

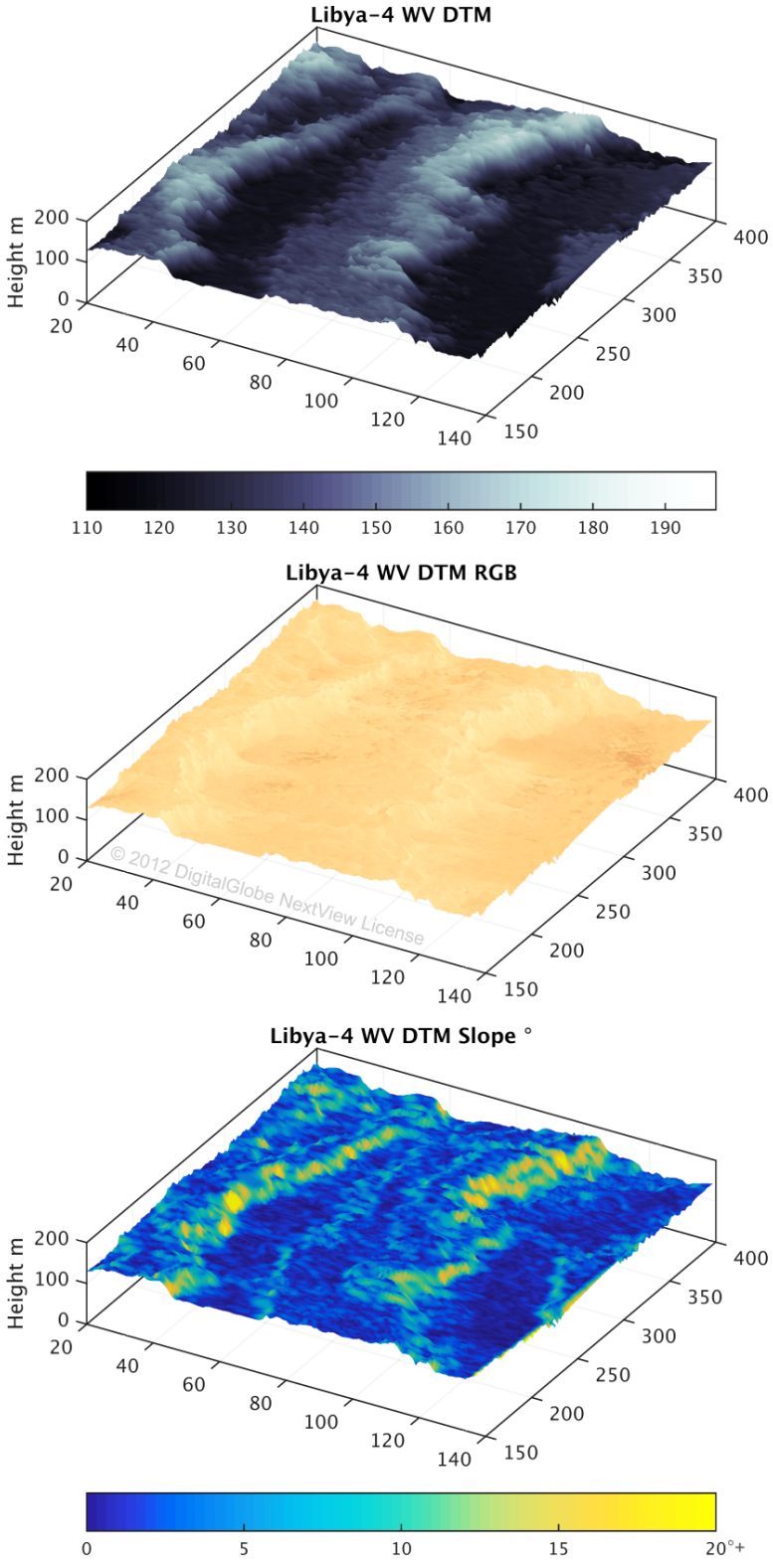
Libya-4 WV DTM
Height m
200
100
0
20
40
60
80
100
120
140
150
200
250
300
350
400
110
120
130
140
150
160
170
180
190
Libya-4 WV DTM RGB
© 2012 DigitalGlobe NextView License
Libya-4 WV DTM Slope °
0
5
10
15
20°+

Fig 2.

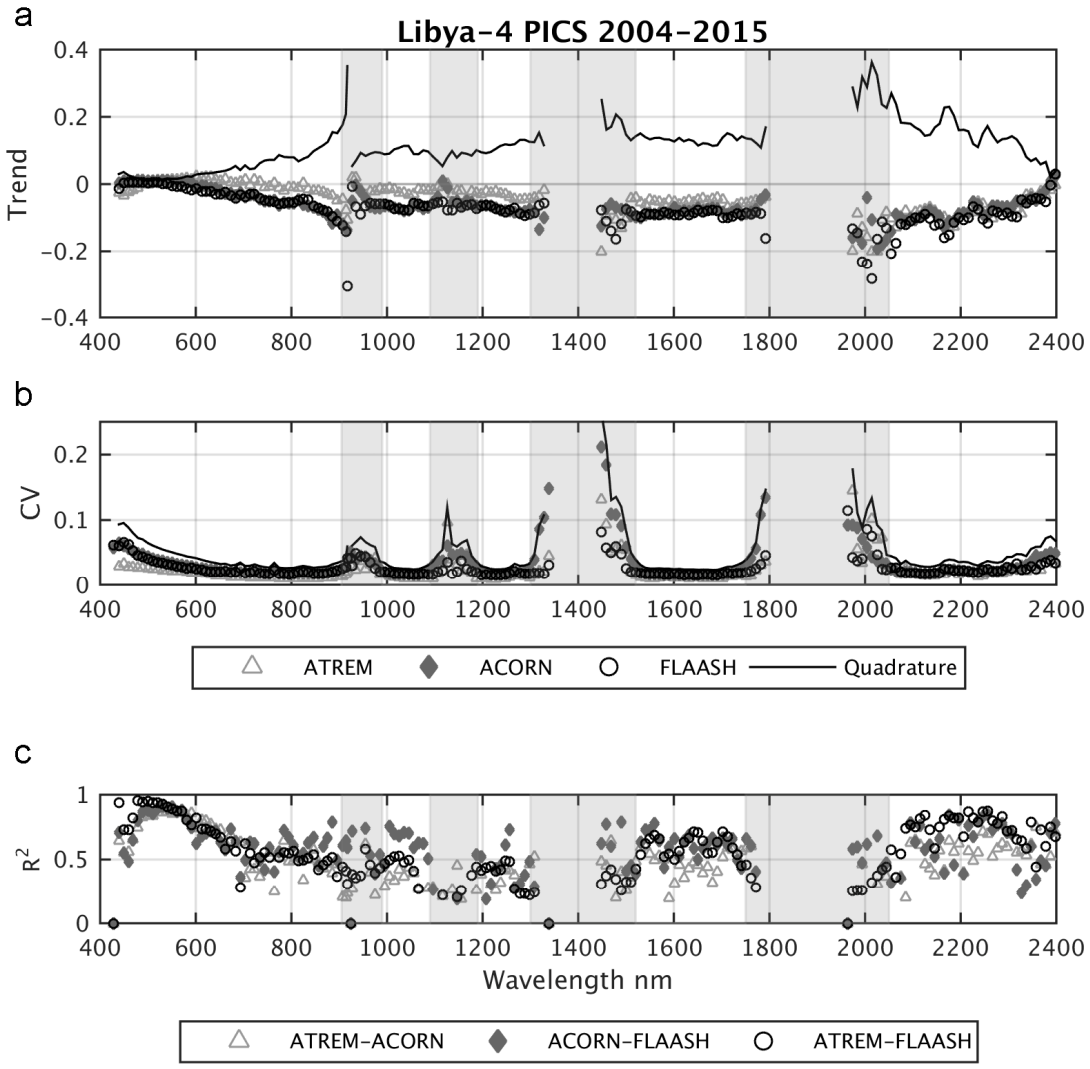
a
Libya-4 PICS 2004-2015
Trend
0.4
0.2
0
-0.2
-0.4
400
600
800
1000
1200
1400
1600
1800
2000
2200
2400
b
CV
0.2
0.1
0
ATREM
ACORN
FLAASH
Quadrature
c
R2
1
0.5
0
Wavelength nm
ATREM-ACORN
ACORN-FLAASH
ATREM-FLAASH

Fig. 3

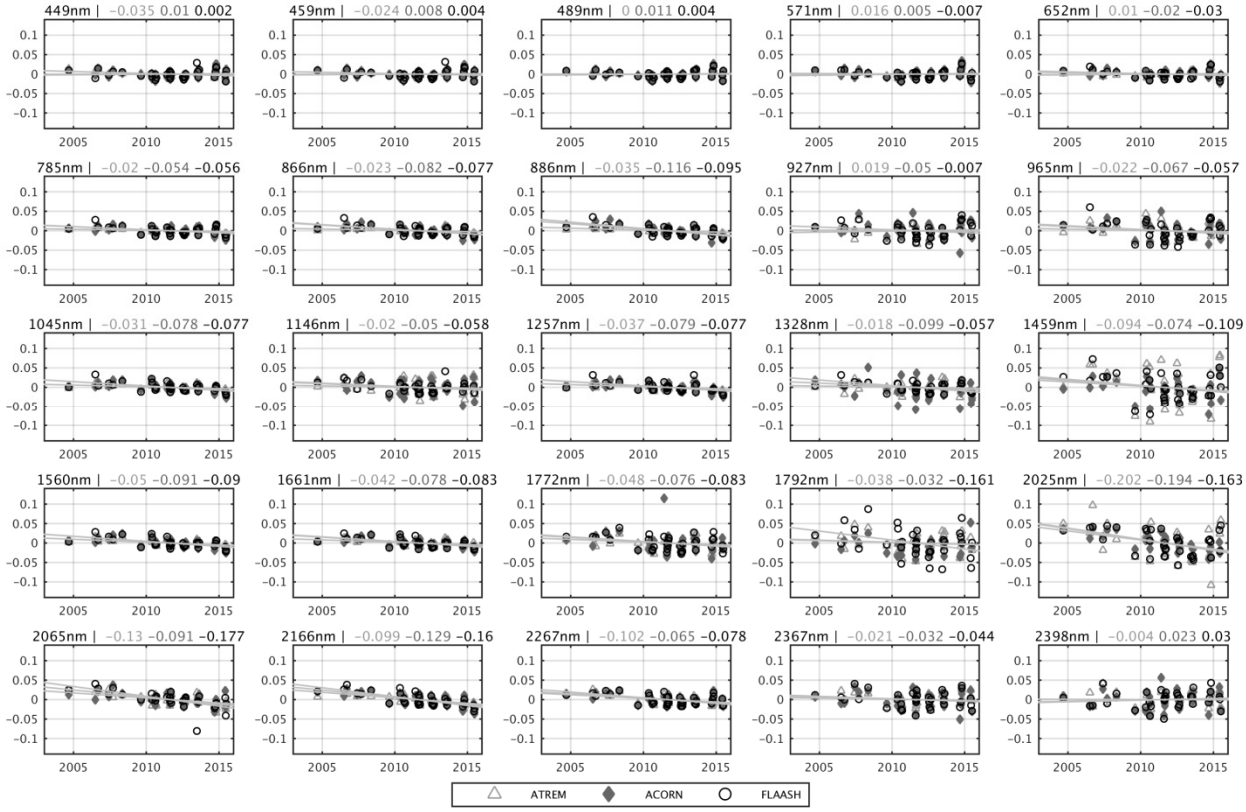
449nm | −0.035 0.01 0.002
459nm | −0.024 0.008 0.004
489nm | 0 0.011 0.004
571nm | 0.016 0.005 −0.007
652nm | 0.01 −0.02 −0.03
785nm | −0.02 −0.054 −0.056
866nm | −0.023 −0.082 −0.077
886nm | −0.035 −0.116 −0.095
927nm | 0.019 −0.05 −0.007
965nm | −0.022 −0.067 −0.057
1045nm | −0.031 −0.078 −0.077
1146nm | −0.02 −0.05 −0.058
1257nm | −0.037 −0.079 −0.077
1328nm | −0.018 −0.099 −0.057
1459nm | −0.094 −0.074 −0.109
1560nm | −0.05 −0.091 −0.09
1661nm | −0.042 −0.078 −0.083
1772nm | −0.048 −0.076 −0.083
1792nm | −0.038 −0.032 −0.161
2025nm | −0.202 −0.194 −0.163
2065nm | −0.13 −0.091 −0.177
2166nm | −0.099 −0.129 −0.16
2267nm | −0.102 −0.065 −0.078
2367nm | −0.021 −0.032 −0.044
2398nm | −0.004 0.023 0.03
ATREM
ACORN
FLAASH

Fig. 4

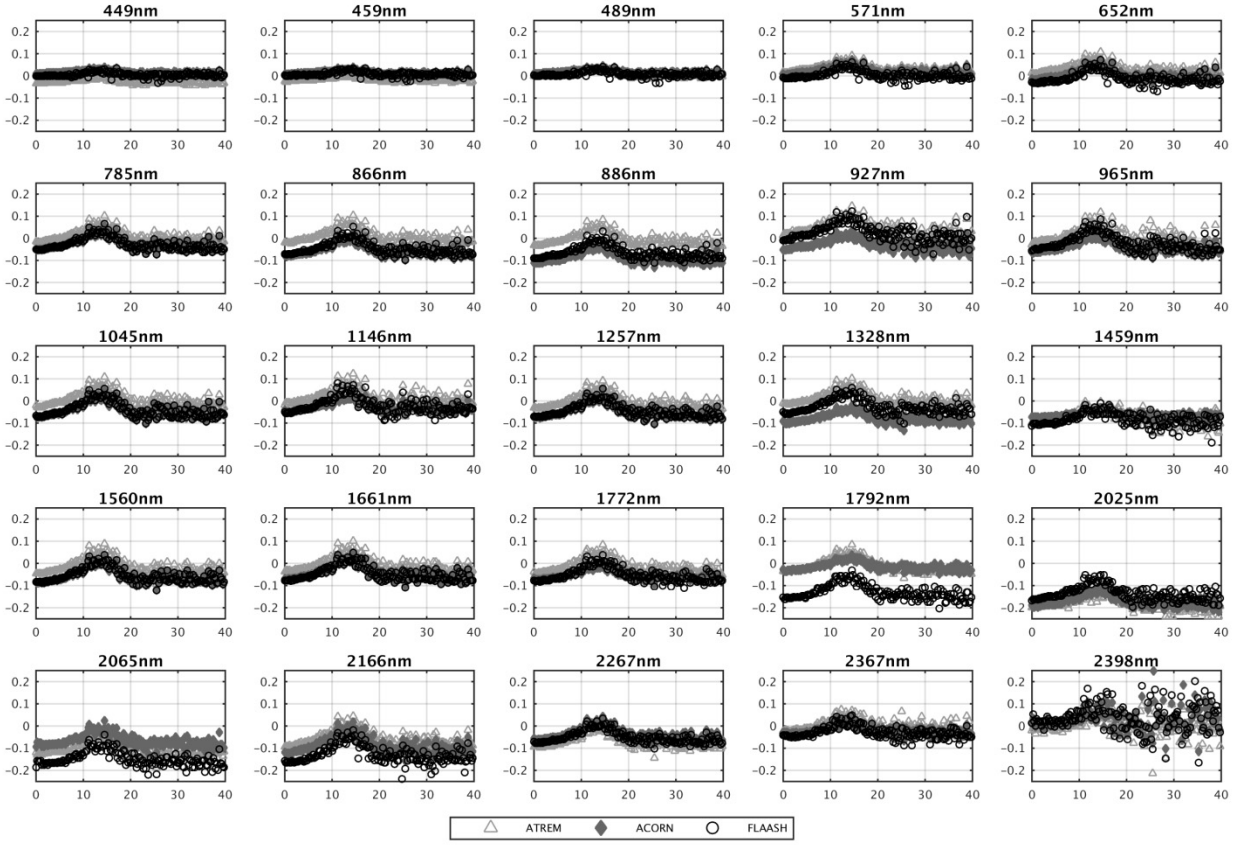
449nm
459nm
489nm
571nm
652nm
785nm
866nm
886nm
927nm
965nm
1045nm
1146nm
1257nm
1328nm
1459nm
1560nm
1661nm
1772nm
1792nm
2025nm
2065nm
2166nm
2267nm
2367nm
2398nm
ATREM
ACORN
FLAASH